ELSEVIER

Contents lists available at ScienceDirect

Surface & Coatings Technology

journal homepage: www.elsevier.com/locate/surfcoat





Inter-relationship of stress and microstructure in BCC and 'beta' tungsten films

Jonathan A. Johnson^a, Tong Su^b, Eric Chason^b, Gregory B. Thompson^a,

- a Department of Metallurgical & Materials Engineering, University of Alabama, Tuscaloosa, AL 35401, USA
- ^b School of Engineering, Brown University, Providence, RI 02912, USA

ARTICLE INFO

Keywords: Beta tungsten Thin film Stress Kinetic model Grain size

ABSTRACT

In this work, a series of W films are deposited at different deposition rates (0.2, 0.5, and 1.0 nm/s) and pressures (0.27, 0.47, 0.67, and 1.33 Pa). Comparing the residual stresses between different deposition rates, the stress was found to become more tensile at higher depositions rates over the pressure ranges studied. Films deposited at the three highest pressures were tensile in stress, had small grains (\sim 15 to 20 nm), and stabilized the metastable A15 phase often referred to as β -W. At the lowest pressure, 0.27 Pa, the films were compressive in stress, larger grain sizes (\sim 70 to 90 nm), and primarily stabilized the body centered cubic α -W phase. If a W seed layer was grown under either the α -W or β -W growth conditions, the subsequent W layer adopted the phase state of the seed layer, independent of processing conditions and/or grain sizes, suggesting that the phase state is most likely determined in the initial stages of nucleation. The seed layer experiment also suggest that these layers can promote more controlled grain sizes in thicker β -W films, which has not been observed in previous work. The stress measurements are interpreted in terms of a previously developed kinetic model that includes effects of growth kinetics, microstructural evolution, and energetic particle bombardment.

1. Introduction

Refractory metals are characterized by their high melting temperature, chemical inertness, and relatively high density. These physical attributes enable them to be resistant to both heat and wear offering a niche material for extreme environments. While refractories are often fabricated through powder metallurgy routes, the use of these materials as coatings has enabled applications as interconnects for semiconductor metallization [1], coatings to mitigate fissile fuel loss in nuclear fuel elements [2], and alternating layers in X-ray mirrors [3]. Film and coating deposition is typically done through chemical vapor deposition (CVD) and magnetron sputter deposition. CVD of refractory films is often carried out utilizing chloride or fluoride precursors, which result in the production of HCl and HF respectively [4]. Because of the environmental health and safety concerns of these byproducts, sputter deposition has become a common tool in the fabrication of refractory films [1–3,5].

Of the refractory metals, tungsten (W) offers the highest melting temperature and is the most isotropic in its physical properties. While it is often reported in its thermodynamic equilibrium body centered cubic (BCC) structure, there are reports of stabilizing a metastable A15 phase,

commonly referred to as β -W, when deposited as a film [5–7]. Such metastable phases have also been reported in other BCC refractory metals when grown as films too [8,9]. This less common β -W phase exhibits a 'giant' spin Hall effect that is beneficial for the development of spintronics [5]. To further develop and systematically engineer this and other W-based film applications, an improved understanding of its growth as a function of deposition conditions is required.

It is well known that deposition parameters determine both the residual stresses and microstructure of deposited films [10]. Understanding how these stresses evolve is important to the development of quality films since residual stress is known to be a dominant factor in the failure of thin films [11]. Delamination and/or buckling of films can be observed when the magnitude of their residual stress is sufficiently large [12]. The generation of such stresses is a complex process with numerous underlying mechanisms that are influenced by the mobility of the deposited adatoms, which is influenced by the deposition technique. For example, sputtering is an energetic deposition process whereas thermal evaporation is not [11]. When adatoms arrive onto a weakly interacting substrate, they diffuse towards one another to form embryonic islands resulting in an initial compressive stress regardless of the adatoms being high or low mobility in nature [13]. This is driven by

E-mail address: gthompson@eng.ua.edu (G.B. Thompson).

 $^{^{\}ast}$ Corresponding author.

surface-to-volume energy considerations. As the islands near each other, the atoms on the surface of the islands elastically strain towards each other to coalesce the islands into a continuous film resulting in a tensile stress state [14]. Since each island has a different crystallographic misorientation to the other, this coalescence ultimately leads to the formation of grain boundaries within the film. For low mobility adatoms, this tensile stress continues after coalescence as the presence of the grain boundaries in the film facilitate the elastic straining between atoms across such boundaries. In high mobility adatoms, a secondary compressive growth regime exists after coalescence, which is less understood. Several models have been proposed to understand and predict the generation of these residual stresses in various material systems [14–17]. In one model, excess adatoms on the film surface are proposed to create the compressive stress [16]. While in another model, it is suggested that adatoms insert themselves into grain boundaries during growth as the film thickens because of a chemical potential difference created between the surface and the grain boundaries under the arriving flux [18].

What is particularly confounding is noting compressive stress formation in refractory metal films. Here, one could expect lower adatom mobility since such metals have higher melting temperatures that translate to higher activation energies for diffusion. Nevertheless, in a high energy deposition technique, *i.e.*, sputtering, the higher mass of refectory atoms can result in energetic bombardment, which is also referred to as ion or atomic peening in the literature. This peening can result in dislocation generation and grain boundary densification that is not typically observed for low mobility adatoms [19,20].

To understand this complex residual stress evolution, Chason and his co-authors developed a kinetic based model that accounts for both the tensile stresses of grain boundary formation and the compressive stress generation of adatom insertion into those boundaries [18,21,22]. The model describes the incremental increase of the average stress integrated over the thickness of the layer due to the additive effects of several stress-generating mechanisms including island coalescence, compressive contributions from the insertion of excess adatoms into grain boundaries, sub-surface grain growth, and energetic peening and bulk defect incorporation. The reader is directed to reference [22] for further details. The ability of this model to accommodate both nonenergetic and energetic growth mechanisms has allowed it to find good agreement with experimental data on sputtered films composed of both high mobility (Cu, Ni) [23,24] and low mobility (Mo) [20,25] adatoms.

While Chason's model has provided good agreement with experimental data in the case of Mo, expanding this model to other low mobility adatom films would be beneficial to promote an improved understanding of stress development in refractory metal films. For example, the stress in W has been reported to deviate with substrate bias [26], temperature [27], sputtering pressure [28,29], and solute alloying [30]. And, as noted earlier, this metal can adopt a metastable β -W phase where little is systematically known in relation to how residual stress evolves when it forms and/or how residual stress may contribute to its stability. This work aims to provide a more complete explanation for stresses generated in W films grown with varying sputtering pressures and deposition rates through the utilization of in-situ stress measure-

2. Experimental and analytical procedure

An AJA ATC-1500 sputtering unit was utilized for balanced magnetron sputtering of the W films analyzed here. This unit was evacuated to a base pressure of $<6.67 \times 10^{-6}$ Pa prior to all depositions. After achieving this base pressure, ultra-high purity Ar was flown into the chamber at a rate of 15 standard cubic centimeter per minute while a gate valve adjusted the pumping speed to maintain the desired deposition pressure. Three W films were grown at different deposition rates (0.2, 0.5, and 1.0 nm/s) at each of the four deposition pressures (0.27, 0.47, 0.67, and 1.33 Pa). To maintain the desired deposition rates over this range of pressures, the films were sputtered either from a single W target or co-sputtered using multiple W targets (up to four) at a target-tosubstrate distance of 16 cm, where all targets had a purity of approximately 99.95 %. As will be developed in the discussion section, W seed layers were also utilized to control a subsequent W film phase state. The processing state of these W seed layers were determined based on the targeted phase state that will be shown in the results section. Prior to each deposition, the deposition rate was measured in-situ utilizing a quartz crystal microbalance. Approximately 270 µm thick Si (100) wafers with a thermally grown 100 nm SiO₂ layer were chosen as substrates and were rotated at 30 rpm during deposition of an approximately 200 nm thick film. All the depositions were performed nominally at room temperature (i.e., without intentional sample heating).

The internal stress values associated with each deposition were measured in-situ using a k-Space Associates® multibeam optical sensor system (MOS) with a data collection frequency of 0.5 Hz. Each measurement is captured when the input trigger is activated by the substrate rotation, which occurs once every full rotation. As the film grows, the substrate bends and the corresponding stress evolution is captured over the deposition time or in other words the film thickness. The MOS laser array is at the center of the substrate positioned between the four equally spaced cathode sputtering guns. As the name suggests, the MOS system utilizes a generated array of lasers spot to measure the curvature of the wafer. This array is generated by passing a single beam laser through a series of two etalons. After generation, the array reflects off the surface of the wafer and is captured by a CCD camera. The mechanical stress generated during the growth of the film is responsible for the bending of the wafer, so measuring the radius of curvature of the wafer allows determination of the magnitude of the stress. This is achieved using the Stoney equation [31,32] described here:

$$\overline{\sigma} = \frac{\kappa M_S h_S^2}{6h_f} \tag{1}$$

where κ is the measured curvature, M_S is the biaxial modulus of the substrate, and h_S and h_f are the substrate and film thickness respectively. All stresses are reported in terms of their stress-thickness product for comparisons.

The residual stress measurements are interpreted by fitting the data to the kinetic model introduced above. The equation describing the evolution of the thickness-integrated stress ($\bar{\sigma}h_f$, referred to as the stress-thickness) is

$$\frac{\mathrm{d}\left(\overline{\sigma}h_{f}\right)}{\mathrm{d}h_{f}} = \sigma_{C} + \left(\sigma_{T,0}\left(\frac{L_{ref}}{L_{o} + \alpha_{2}h_{f}}\right)^{\frac{1}{2}} - \sigma_{C}\right)e^{\left(-\frac{\beta D}{R\left(L_{o} + \alpha_{2}h_{f}\right)}\right)} + M_{f}\Delta a \frac{\alpha_{1}h_{f}}{\left(L_{o} + \alpha_{1}h_{f}\right)\left(L_{o} + \alpha_{2}h_{f}\right)} + \frac{1}{L_{o} + \alpha_{2}h_{f}}A_{0} + \left(1 - \frac{1}{L_{o} + \alpha_{2}h_{f}}\right)\frac{B_{0}}{\left(1 + \frac{1}{R\tau_{s}}\right)}$$
(2)

ments with such data fitted to Chason's model to further expand experimental assessment of this model.

with several adjustable and experimental parameters. The first two term corresponds to the stress in the film during non-energetic growth and

encompasses a tensile contribution from island coalescence and a compressive component from the insertion of excess adatoms into grain boundaries with σ_C and $\sigma_{T,0}$ being the parameters determining the compressive and tensile stresses, respectively. The βD is a parameter dependent on the concentration and mobility of surface atoms. The third term corresponds to the effect of sub-surface grain growth where $M_f \Delta a$ is related to the densification associated with subsurface grain growth. M_f is the biaxial modulus of the film and Δa is the width of the grain boundary. The last two terms correspond to stress from the energetic growth mechanisms of energetic peening and bulk defect incorporation, respectively. Here A_0 is an adjustable parameter fitting the model to experimental data that is dependent on the working pressure, l is a distance utilized to determine the fraction of energetic particles that induce stress at the grain boundaries, B_0 is the stress due to the steady state concentration of bombardment-induced defects in the film, and τ_s is the characteristic time for a defect to diffuse to the surface and annihilate, which can be determined from $\sqrt{D_i \tau_s} = l + R \tau_s$. R is the growth rate and L_{ref} is a reference grain size (taken as 1 nm). L_{ref} is used to make $\sigma_{T,0}$ have units of stress. By taking L_{ref} as 1 nm, it allows (L_{ref}/L_h) to be dimensionless and not affect the value of the fit. The grain size is assumed to change linearly with the deposited thickness, where L_0 + $\alpha_1 h_f$ describes the grain size at the film-substrate interface and $L_0 + \alpha_2 h_f$ is the grain size at the film surface.

A MatLab® code was written to determine the parameters based on a non-linear least-squares algorithm for fitting Eq. 2 to the experimental input data. In the fitting, some parameters $(\sigma_T, 0, \beta D \text{ and } M_f \Delta a)$ are set to be common for all the deposition condition while others $(\sigma_C, L_0, \alpha_1 \text{ and } \alpha_2)$ are allowed to vary for the different processing conditions within different data sets. To reduce the number of fitting parameters, the energetic parameters $(A_0, B_0 \text{ and } I)$ are assumed to depend linearly on pressure below a threshold of P_0 so that $A_0 = A^* (1 - P / P_0)$ where A^* and P_0 are fitting parameters that are common for all the data. The same linear pressure dependence is assumed for B_0 and I. Since the deviation between the model and the data is not only because of experimental error, the error associated with each parameter cannot be determined precisely. The fitting parameters determined should be thought of as a reasonable set of values but not uniquely correct. Additional details of the model and fitting procedure can be found in [18,21,22].

To support the model input parameters, post-growth characterization was done to quantify the film microstructure. The phase of each film was determined utilizing X-ray diffraction (XRD) on a Bruker D8 Discover with a Co K_{α} source over a 2θ range of 30 to 120° . The grain size at each film surface was determined by one of two techniques depending on the size regime of the grains. Grain size measurements for small grains were achieved using transmission electron microscopy (TEM) in the plane-view (normal to the growth surface). These specimens were prepared by dimpling 3 mm diameter discs of $<100~\mu m$ thickness to a thickness of $<15~\mu m$ with a Fischione model 200 dimple grinder from the substrate side. These discs were then ion milled using a Gatan

Precision Ion Polishing System until perforation enabling electron transparency around the holes. Cross-sectional samples of the films were prepared by a focus ion beam (FIB) milling lift-out technique [33] in a Lyra Tescan FIB. If the deposited film grains were sufficiently large (>50 nm), electron backscatter diffraction (EBSD) from the film surface was carried out with an EDAX detector in a ThermoFisher Apreo by scanning electron microscopy (SEM). Through EBSD, grain maps and subsequent analysis were completed using the OIM Analysis v7 platform. Grain dilation was performed as a multi-iterative procedure with a minimum tolerance angle and grain size of 5° and 10 nm, respectively.

3. Results

In-situ stress measurements collected for different processing conditions using the MOS system are provided in Fig. 1. The data presents the average stress thickness value for each W film as a function of its thickness. Fig. 1(a–c) each represent a different deposition rate (0.2, 0.5, and 1.0 nm/s respectively) and contains data for all four deposition pressures (0.27, 0.47, 0.67, and 1.33 Pa) for the given rate. Because of the fast growth rates and the limited substrate rotation speed (which determines the rate of data collection), the initial stress response of the films at the early stages of growth are not captured and explains the lack of stress convergence to zero at zero thickness. Regardless, comparing the data from all three rates reveals that the general trend of the stress response does not change as a function of deposition rate. However, it can be observed that the lower deposition rates tend to drive the stress magnitudes towards more compressive values.

Altering the deposition pressure results in a more complex stress response trend evident by the larger stress differences between films grown over these pressures. The three highest pressures (0.47, 0.67, and 1.33 Pa) follow a common trend where the stress displays more tensile values as the pressure is lowered. In contrast to this trend, films grown at the lowest pressure, 0.27 Pa, experience extreme compressive stresses. This suggests a fundamental difference between the films grown at 0.27 Pa and the remaining pressures. Furthermore, the linear slopes observed after initial stress generation suggest that the incremental stress does not change as a function of the film thickness, *i.e.*, the grains are not growing substantially during deposition [13].

One factor that should be considered to explain the difference in stress response at 0.27 Pa is a change in the phase of the W films. As mentioned in the introduction, W is commonly observed in its α or BCC phase but sputtering has been reported to stabilize the A15 β phase over a range of deposition parameters [5–7]. Furthermore, previous research in determining the stress response of the β -W phase has shown that it tends to promote tensile stresses [26,30]. To elucidate how each film's phase may relate to its growth stress, XRD patterns are provided in Fig. 2. In this data, the non-labeled peaks were determined to be from the substrate. Fig. 2(a) displays the patterns associated with the tensile films. As with the previous work, it is found that deposition parameters

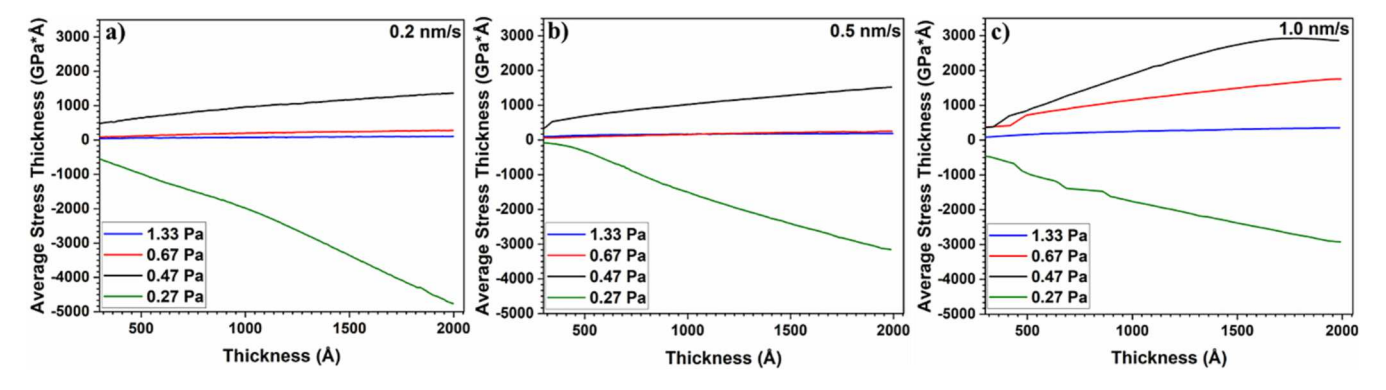


Fig. 1. In-situ growth stress evolution of W films sputtered with deposition pressures of 0.27, 0.47, 0.67, and 1.33 Pa at deposition rates of (a) 0.2 nm/s, (b) 0.5 nm/s, and (c) 1.0 nm/s.

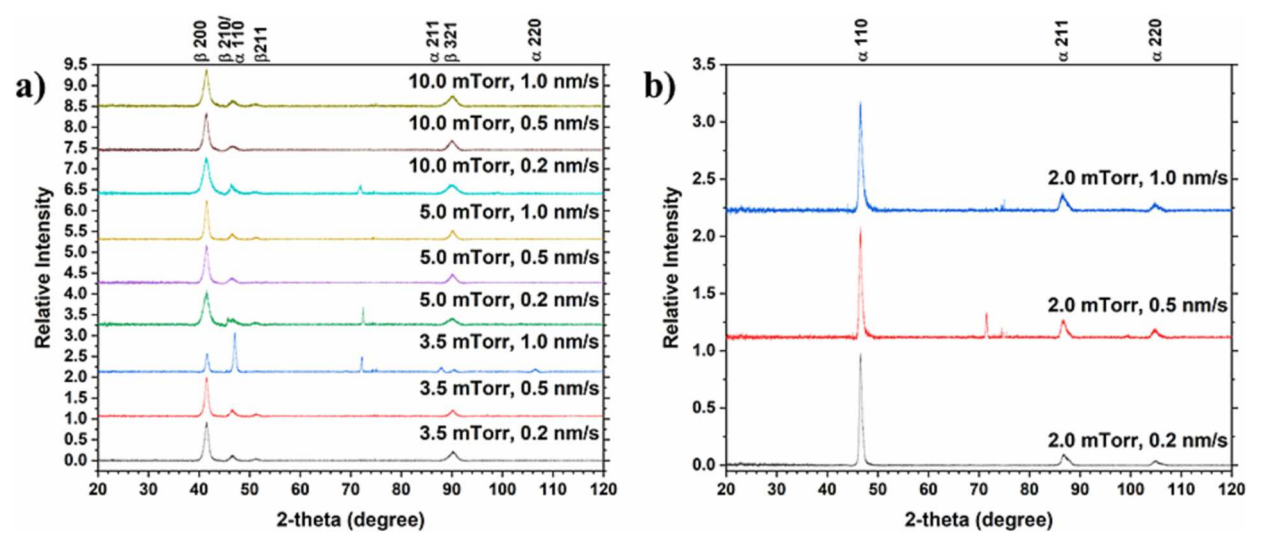


Fig. 2. XRD patterns for films deposited across all deposition parameters. (a) Patterns associated with films displaying tensile stresses show stabilization of the β-W in all cases. (b) Patterns from the compressive films suggest only BCC or α -W formation. Unlabeled peak at \sim 72° is attributed to the Si (400) peak.

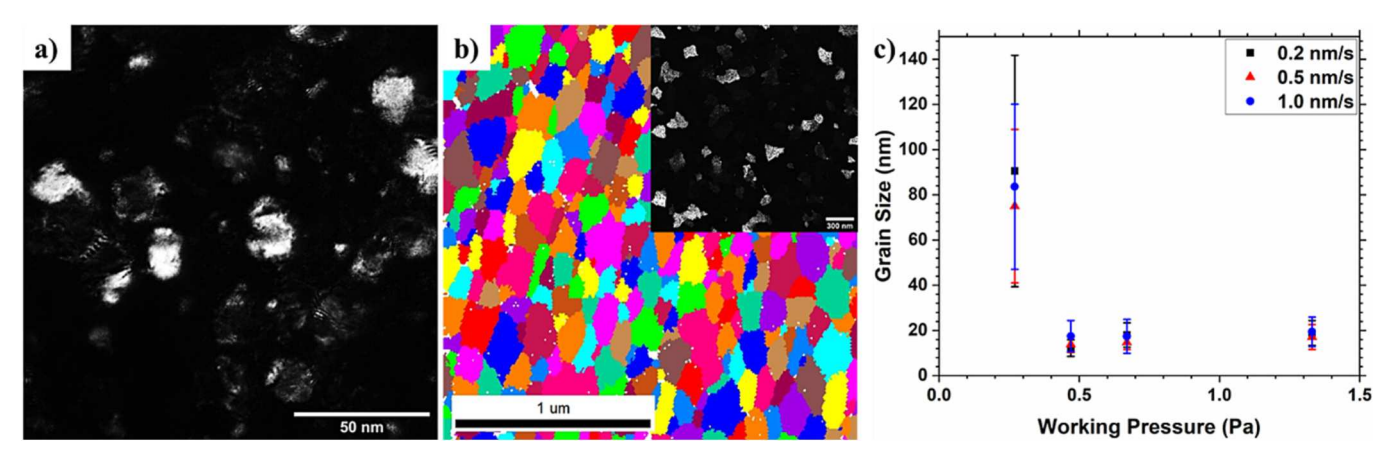


Fig. 3. (a) Representative dark field TEM micrograph utilized for grain size determination in β -W films (0.5 nm/s and 0.67 Pa). (b) Representative EBSD grain map utilized for grain size determination in α -W films with inset dark field micrograph (0.5 nm/s and 0.27 Pa). Note the grain map provided utilizes random colors to identify grains and is not texture dependent. (c) Figure detailing the grain sizes determined for all films based on deposition pressure and rate.

leading to tensile stresses also promote the formation of β -W. Meanwhile, Fig. 2(b) shows that films with compressive stresses are deposited in only the BCC structure. This suggests that the deposition pressure strongly influences the final phase of the film. Of particular interest is the film grown at 1.0 nm/s at a pressure of 0.47 Pa, as it was the only film to exhibit formation of both α and β -W phases. This would suggest that stabilization of the β phase is a function of both the deposition

Table 1A condensed summary of the deposition rate, working pressure, stress states, phases, and grain sizes of each W film.

Rate (nm/s)) Pressure (Pa) Stress star		Phase	Grain size (nm)
0.2	0.27	Compressive	α	90.5 ± 51.2
0.2	0.47	Tensile	β	12.2 ± 3.7
0.2	0.67	Tensile	β	18.0 ± 5.4
0.2	1.33	Tensile	β	18.9 ± 5.5
0.5	0.27	Compressive	α	75.0 ± 34.0
0.5	0.47	Tensile	β	13.9 ± 3.7
0.5	0.67	Tensile	β	14.7 ± 3.1
0.5	1.33	Tensile	β	17.1 ± 5.5
1.0	0.27	Compressive	α	83.6 ± 36.5
1.0	0.47	Tensile	α/β	17.5 ± 6.9
1.0	0.67	Tensile	β	17.4 ± 7.5
1.0	1.33	Tensile	β	19.4 ± 6.5

pressure and rate since other films were grown at this pressure but only stabilized the β phase, which is consistent with prior reports [5,34].

The grain size analysis performed reveals a fundamental difference in the structure of the tensile and compressive W films. Fig. 3 provides an overview of this analysis. For the smaller grain sized films, which corresponds to the tensile-stress state $\beta\text{-W}$ films, dark field TEM, Fig. 3(a), reveals them to be $\sim\!15$ to 20 nm in size. In contrast, the highly compressive $\alpha\text{-W}$ films were $\sim\!70$ to 90 nm, confirmed by the EBSD grain map, Fig. 3(b). The collective comparisons of the grain sizes are plotted in Fig. 3(c) and tabulated in Table 1 along with the phase state, stress state, and processing state for each film. These grain size measurements provide an independent determination of the parameter L that is used in the stress model.

Using the stress measurements from Fig. 1, the data was fit to the kinetic model. The resulting best-fit parameters are tabulated in Table 2. The first part of Table 2(a) are parameters that are held common for all the processing conditions and regardless of the phase (α or β) present within the film. Meanwhile, the second part, Table 2(b), are the parameters that depend on the processing conditions, *i.e.*, R, T and P (shown in columns 2–4). The 6th column is the average grain size calculated from the fitting parameters at 200 nm, *i.e.*, the thickness at which the grain size was measured using $L_{ave} = L_0 + \frac{1}{2}(\alpha_1 + \alpha_2)*200$,

Table 2

(a) Fitting parameters that are common to all the processing conditions. (b) Fitting parameters that are different for each set of processing condition.

a)

Fitting Parameters Common to All Files							
$\sigma_{T,0}$ (GPa)	$\beta D \\ (T = 300K) \\ (nm^2/s)$	<i>Mf∆α</i> (GPa*nm)	Di (nm²/s)	Р ₀ (Ра)	A* (GPa)	<i>B</i> * (GPa)	<i>l</i> * (nm)
3.161	6E-9	40.788	0.239	0.518	-8.127	-11.57	0.624

b)

Color	R (nm/s)	P (Pa)	σ _c (GPa)	L_0 (nm)	(200 nm) (nm)	α1	α2
	1	0.27	-4.0	12.0	20.6	0.043	0.043
	0.5	0.27	-4.0	22.2	29.6	0.037	0.037
	0.2	0.27	-4.0	28.3	68.5	0.001	0.401
	0.2	0.47	-4.0	28.8	30.8	0.000	0.020
	0.5	0.47	-4.0	17.7	19.7	0.000	0.020
	1	0.47	-4.0	3.8	12.9	0.020	0.071
	1	0.67	-4.0	20.7	22.9	0.002	0.020

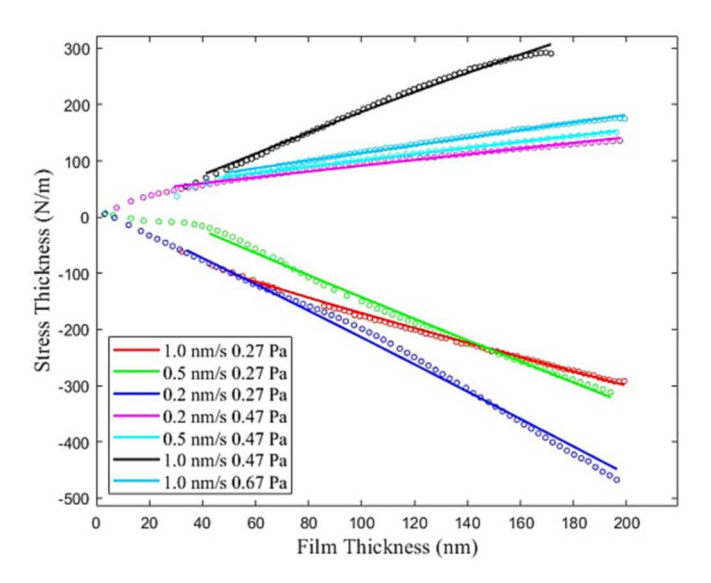


Fig. 4. Kinetic model fitting results (solid line) and experimental data (circles) for stress-thickness evolution with thickness.

where 200 is the film thickness in nm. Note the values of L_{ave} and α_2 are much larger for the film grown at 0.27 Pa and 0.2 nm/s than other conditions; this is contributed to the increased grain growth because of the combination of the low pressure and growth rate. This is further

supported by Fig. 3 and Table 1, as this condition provides the largest grain size. Using these parameter values, the resulting stress-thickness is plotted in Fig. 4 with the experimentally measured data represented by the circular symbols and the fit by the solid lines. The color in Fig. 4 corresponds to the color in the first column of Table 2(b) to facilitate direct comparison. Note that the data taken at 1.33 Pa for R=0.2, 0.5 and 1 nm/s and 0.67 Pa for R=0.2 and 0.5 nm/s (near zero stress response, Fig. 1) were not fitted to the model because the TEM images (see Appendix A) revealed large gaps between the grains. Such gaps are not consistent with the assumptions of the model that the films are continuous.

4. Discussion

The results shown above detail the importance of both the sputtering rate and pressure on the characteristics of W films, as altering these parameters led to changes in their stress states, grain sizes, and phases. The discussion moving forward aims to elucidate the underlying mechanisms that contribute to these differences.

When considering the stress response of films grown with different process parameters, both deposition rate and working pressure determine the final stress response. The interaction between them may be complex, as shown by the trends in the data shown in Fig. 4. For instance, increasing the deposition rate for low energy growth (i.e., high pressure or evaporation) typically results in more tensile stress responses. On the other hand, the stress typically becomes more compressive for higher growth rates when the particles have higher energy (i.e., lower pressure) [23,35]. The kinetic model is able to

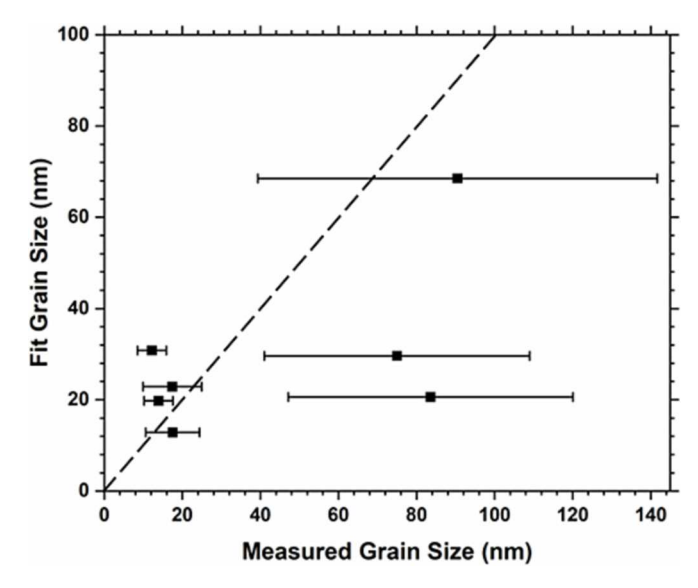


Fig. 5. Correlation of the measured grain size and fitted grain size at h = 200 nm. The dashed line represents y = x or in other words a perfect fit agreement.

account for these observations by including the deposition-rate dependence of both the growth kinetics and energetic particle bombardment. For low energy, high deposition rates, it provides less time for insertion of surface adatoms into the developing grain boundaries [23,36] which reduces the compressive stress. For higher energy, higher deposition rates, it traps more defects that generate more compressive stress.

While the growth rate offers some ability to tune stresses within the films, working pressure is found to play a more significant role in determining whether the W films grow dominantly tensile or compressive. This is evident by the film developing more compressive stress (Fig. 1) when lowering the working pressure from higher values (0.47, 0.67, or 1.33 Pa) to the lowest value (0.27 Pa). The model also agrees with this trend by incorporating energetic bombardment as a mechanism of stress generation in which the energetic parameters become larger at lower pressure. This model has similarly been applied to the deposition of Mo films, a similar refractory film to W, where this pressure dependence on compressive stress in relationship to the energetic peening effect is also observed [22,25]. Similarly, this phenomenon may explain the initial tensile increase in stress associated with lowering the pressure from 1.33 to 0.47 Pa because the energetic bombardments provide additional energy to eliminate the voids observed in the higher pressure films. Eliminating these voids allows for the formation of grain boundaries, which as discussed in the introduction is a large tensile contributor to film stress. This is further supported by the images provided in Appendix A that show a smaller fraction of voids at 0.47 Pa when compared to 1.33 Pa.

To understand why the energetic bombardment mechanism contributes more at lower pressures, it is important to understand that adatoms lose energy based on gas phase collisions during the sputtering process. The probability of such gas phase collisions can be understood by the number of successive particle collisions determined by the mean free path of the sputtered atom from the target to the substrate. The mean free path approximation, λ , is given by the following equation:

$$\lambda = \frac{k_B T}{\sqrt{2}\pi (r_g + r_m)^2 P} \tag{3}$$

where k_B is Boltzmann's constant, T is temperature, r_g and r_m are the covalent radii of the gas and sputtered ion respectively, and P is pressure [7]. Using Eq. 3, λ for the lowest to highest pressures range from 2.5 to 0.5 cm. As the pressure decreases, the mean free path increases resulting in less gas phase collisions that equates to lower energy loss. In terms of

the energetic bombardment mechanism, this allows the incoming adatoms to impact the growing film with higher energies that result in more compressive stress generation.

Grain size of the films is also found to change significantly when lowering the working pressure. Fig. 3(c) reveals that all the tensile highpressure films exhibit a small grain size on the order of 15 to 20 nm, which follows the grain morphology of small, columnar grains predicted by the Thornton structure zone model [35]. In Thornton's model, low mobility adatoms associated with deposition of W films, at ambient temperature, would promote the formation of a Zone 1 structure. For these films, we even note voiding between the columnar grains (see Appendix A), which is again consistent with the Thornton model. However, the compressive films reveal larger grain sizes of 70 to 90 nm, Fig. 3(b). While the larger grain sizes observed in the low-pressure films are more indicative of a Zone 2 structure in the Thornton model, the ambient temperature during deposition is predicted to promote the Zone 1 structure regardless of deposition pressure [35]. Nevertheless, these larger W grain sizes, at low pressures, have been reported in previous work [7,36]. In both references, the increase in grain size was attributed to the introduction of higher energy bombardments during growth promoting coarsening.

For further examination of this grain growth effect, the measured grain size (Fig. 3c) and the grain size predicted from the modeling are compared in Fig. 5. The grain size was calculated from the fitting parameters for the same thickness at which the measurements were done (i.e., 200 nm). While the fit does not show complete agreement with the measured grain sizes, the values are similar in magnitude, which supports the suggestion that the increase in the magnitude of energetic bombardment is the primary mechanism for the differences observed between the grain sizes at high and low pressures. In contrast to working pressure, the deposition rate is found to have only limited effect on the grain sizes (Fig. 3(c)), which challenges the typical notion that grain size should decrease with increasing deposition rate because of the limited time for adatom coalescence [37]. This can be attributed to the W adatoms not having sufficient mobility to coalesce irrespective of deposition rate.

The differences in film stress and grain structure observed between high- and low-pressure films may play a strong role in determining which phase of W is stabilized. Catania *et al.* [38] reported experimental studies between α and β Ta films and stated that the compressive stress trended with the higher density phase, *i.e.*, the β -Ta film. They further noted that W has an opposite phase density, or, in other words, β -W is

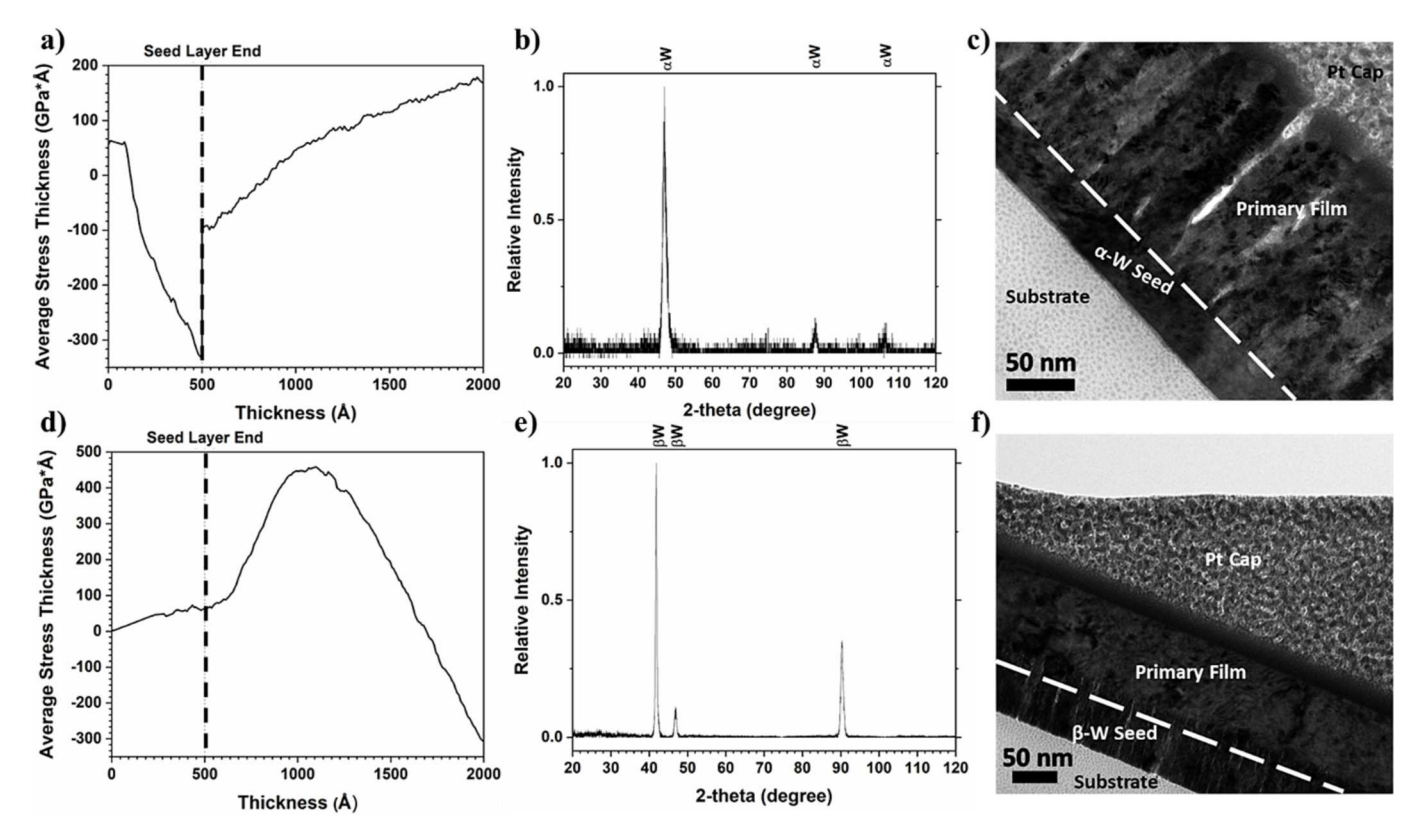


Fig. 6. (a) In-situ stress growth evolution of a W film grown at 0.5 nm/s with the seed layer grown at 0.27 Pa and the secondary layer grown at 1.33 Pa. (b) XRD showing α -W formation in the film from part (a). (c) Cross-sectional TEM micrograph of film from parts (a) and (b) showing distinct grain morphology in each layer. (d) In-situ stress growth evolution of a W film grown at 0.5 nm/s with the seed layer grown at 1.33 Pa and the secondary layer grown at 0.27 Pa. (e) XRD showing β-W formation in the film from part (d). (f) Cross-sectional TEM micrograph of film from parts (d) and (e) showing distinct grain morphology in each layer.

less dense than α -W. They concluded that for W films, compressive stress would then favor the α-W phase. Further work by Vüllers and Spolenak [7] highlights that the level of voiding within a W film may also result in the formation of β -W. The β -W phase has been reported to be stabilized by residual oxygen [39,40]. Vüllers and Spolenak claim that the voids allow easier interaction with residual oxygen within the chamber resulting in stabilization of this phase. In a prior paper by the authors [30], we reported the residual oxygen in W films grown in the same chamber here to be <0.9 at.% when the base pressure was \sim 1.33 \times 10^{-5} Pa. In this work, we achieved an even lower base pressure prior to deposition of $\sim 6.67 \times 10^{-6}$ Pa. Regardless, it is worth noting that all films directly deposited onto the substrate that formed β -W had some varying amount of voiding found in the microstructure which was absent in the α -W film (see Appendix A). The question of whether compressive stresses or a voided microstructure are required to form the β -W is expanded upon later in the discussion.

Besides stress state and potential voiding as a contributor to β -W stability, the deposition rate may also play a role in phase stabilization of the W films. For example, all the deposition rates where the film grew tensile adopted the β -W phase except for the film at the highest rate, 1.0 nm/s, at 0.47 Pa, which was a mixture of both the α and β -W phases, Fig. 2(a), and retained the tensile stress state, Fig. 1(a). As the pressure increased to 0.67 Pa at 1.0 nm/s, the film reverted to being only β -W for all equivalent and higher pressures at this rate.

With the trends discussed this far, it is clear the deposition pressure, stress state, phase of the W film, morphology of the film (voiding), and grain sizes are all interconnected. To decipher these interconnections, an additional set of experiments was undertaken. Here, a seed layer was grown under one condition to stabilize a specific W phase with the subsequent film grown on the seed surface but at a different growth

condition to stabilize the other W phase. Whether the W layer was the seed or the subsequent layer grown on the seed, the β -W conditions were 0.5 nm/s at a pressure of 1.33 Pa and the α -W conditions were 0.5 nm/sat a pressure of 0.27 Pa. The results of these two experiments are presented in Fig. 6, where (a)–(c) represents the β -W film parameters on the α -W seed and (d–f) represent the α -W film parameters on the β -W seed. In both cases, the stress states of the primary films are seemingly unaffected by the seed layer. The layers grown at 1.33 Pa (the β condition) always results in tensile stress and the layers grown at 0.27 Pa (the α condition) ultimately results in compressive stresses (see Fig. 6(a) and (d)). The tensile jump at 50 nm in Fig. 6(a) is attributed to relaxation of the film during a lack of deposition as the process parameters were changed to deposit the second layer. The initial large tensile increase in incremental stress, as evident by the change in slope, observed after the seed layer deposition in Fig. 6(d) is attributed to the closure of voids resulting in grain boundary formation in the secondary layer of the film in its early stages of growth. Fig. 6(b) and (e) show that the phase of the subsequent films is dependent on the phase of the seed layer from which it grows. An α -W seed layer promotes the α phase in the entire film even when depositions parameters that led to the prior β -W stabilization are used (Fig. 6(b) and vice-versa for the β -W seed layer where the subsequent W film adopts the A15 structure even though the parameter would suggest bcc growth (Fig. 6(e)). While the seed layers stabilize the phase of the film, they do not stabilize the grain structure of the film, as seen in Fig. 6(c) and (f). All layers grown at 1.33 Pa show small columnar grains with voided boundaries while the 0.27 Pa produced larger, densified columns

The results of these seed layer experiments provide improved insight into the interconnections of the deposition pressure, stress state, phase state, and grain size. The independence of both the stress state and grain

size from the seed layer reveals that these are likely altered by the processing conditions themselves rather than the film's phase. This discovery provides new understanding in that the increase in energy of the bombarding particles is the primary cause of both the large grains and compressive stresses observed in the low-pressure films and not the film's phase. Secondly, the dependence of the film's phase on the seed layer suggests the importance of phase stability in the early stages of growth on the surface which it grows from. Previously, the stabilization of the β -W phase was rationalized by the ability of oxygen to easily migrate into a film through porosity found in the microstructure [7]. In contrast, Fig. 6(e) and (f) shows densified grains but for a film that is β -W. While this does not disprove the claims of Catania et al. [38] or Vüllers and Spolenak [7], it does suggest that compressive stresses and voided microstructures are not necessarily requisite for β-phase stabilization. Rather, the stabilization of phases by seed layers suggests that the dominating phase is largely dependent on the initial stages of its growth. For example, interactions with residual oxygen during nucleation of the films may be the primary influence on the final stabilized phase, which has been proposed in the stabilization of metastable tantalum films [8,9,41]. Other than the possible minute oxygen presence discussed above in this chamber, it appears that the energy of these depositing adatoms likely provides the primary reason for the formation of β-W in these sputter-deposited films since this phase was stabilized over a variety of different processing conditions (pressures and rates). In those cases, the deposition energy of the arriving adatoms was insufficient to promote the formation of the thermodynamically stable α -W phase [7,28]. Finally, this work provides potential new routes for production of densified β -W which, to the authors' knowledge, has not been observed previously. Such findings may enable further functionality control for films in spintronics applications [5] and other potential applications where β -W is found to be beneficial.

5. Conclusion

A series of W films were deposited by magnetron sputtering to determine the effects of both deposition rate and pressure on the stress states and microstructure of the films. An experimental matrix composed of three growth rates (0.2, 0.5, and 1.0 nm/s) and four deposition pressures (0.27, 0.47, 0.67, and 1.33 Pa) was constructed. *Insitu* stress analysis, XRD, and TEM/EBSD were utilized to determine the stress states, phases, and grain sizes of the films, respectively. For films deposited at 0.27 Pa, regardless of the deposition rate, the films were bcc α -W and compressive in stress with grain sizes $\sim\!\!70$ to 90 nm. Films grown at 0.47, 0.67, and 1.33 Pa were found to have tensile stresses, grain size $\sim\!\!15$ to 20 nm, and the stabilization of the A15 β -W phase. These results demonstrated that deposition pressure, stress state, grain size, and phase were all interconnected.

Using a seed layer experiment, where the seed was grown at a condition to stabilize the aforementioned films with the subsequent layer grown under an opposite phase condition process, it was found that the seed layer, not the process state, stabilized the phase for the conditions studied. As a result, the $\beta\text{-W}$ film was densified and adopted a larger grain size. Alternatively, the film stress depended primarily on the processing conditions and not the underlying seed layer. These results indicate that the stress state and grain size are primarily dependent on the sputtering pressure and not the phase, with the phase determined during the initial stages of nucleation from the surface from which it grows off. This also provides an avenue for promoting both fine and coarse grain structures in $\beta\text{-W}$ films, which has not been previously reported.

As stress state and grain size depend heavily on sputtering pressure, the distinct differences observed between high and low-pressure films is attributed to the increased energy of depositing adatoms at low pressure providing an increased energetic peening effect on the films surface. To further understand the contributions of energetic peening and other mechanisms to the film stress state, a kinetic growth model was utilized. Using reasonable setting of the processing parameters, the model was able to simulate multiple data sets under different deposition conditions with good agreement to the experimental data. Collectively, these findings provide further understanding to both the growth conditions for residual stress evolution as well as the stabilization of $\beta\textsc{-W}$ in the thin film form.

Credit authorship contribution statement

Conceptualization of the process completed by JAJ and GBT. JAJ completed the film growth, experimental characterization, and original draft preparation with edits by all coauthors. TS and EC provided insight into the kinetic modeling and fit the experimental data to said model. GBT and EC acquired respective funding for the project. All authors have read and agreed to the published version of the manuscript.

Declaration of competing interest

The authors declare that they have no known competing financial interests or personal relationships that could have appeared to influence the work reported in this paper.

Data availability

Data will be made available on request.

Acknowledgments

JAJ and GBT recognize the NASA Early-Stage Innovations grant 80NSSC18K0255. The effort of EC was supported by the National Science Foundation (NSF) under Contracts No. DMR-1602491 and DMR-2006422 and TS by DMR-2006422. The authors thank Zhaoxia Rao for initial discussions and preliminary fittings of the kinetic model to W films.

Appendix A

As stated previously, the data taken at 1.33 Pa for R=0.2, 0.5 and 1 nm/s and 0.67 Pa for R=0.2 and 0.5 nm/s were not fit to the model because TEM images revealed large gaps between the grains, and the model assumes a consolidated film. Fig. A.1 provides the requisite bright field TEM micrographs utilized to determine the level of voids present within the films grown at pressures of 0.47, 0.67, and 1.33 Pa. Fig. A.2 provides a representative bright field micrograph of the films grown at 0.27 Pa that highlights the fully consolidated nature of the films. Micrographs for each of the films grown at 0.27 Pa are not provided because the large compressive stresses limited the ability to produce plane-view specimens.

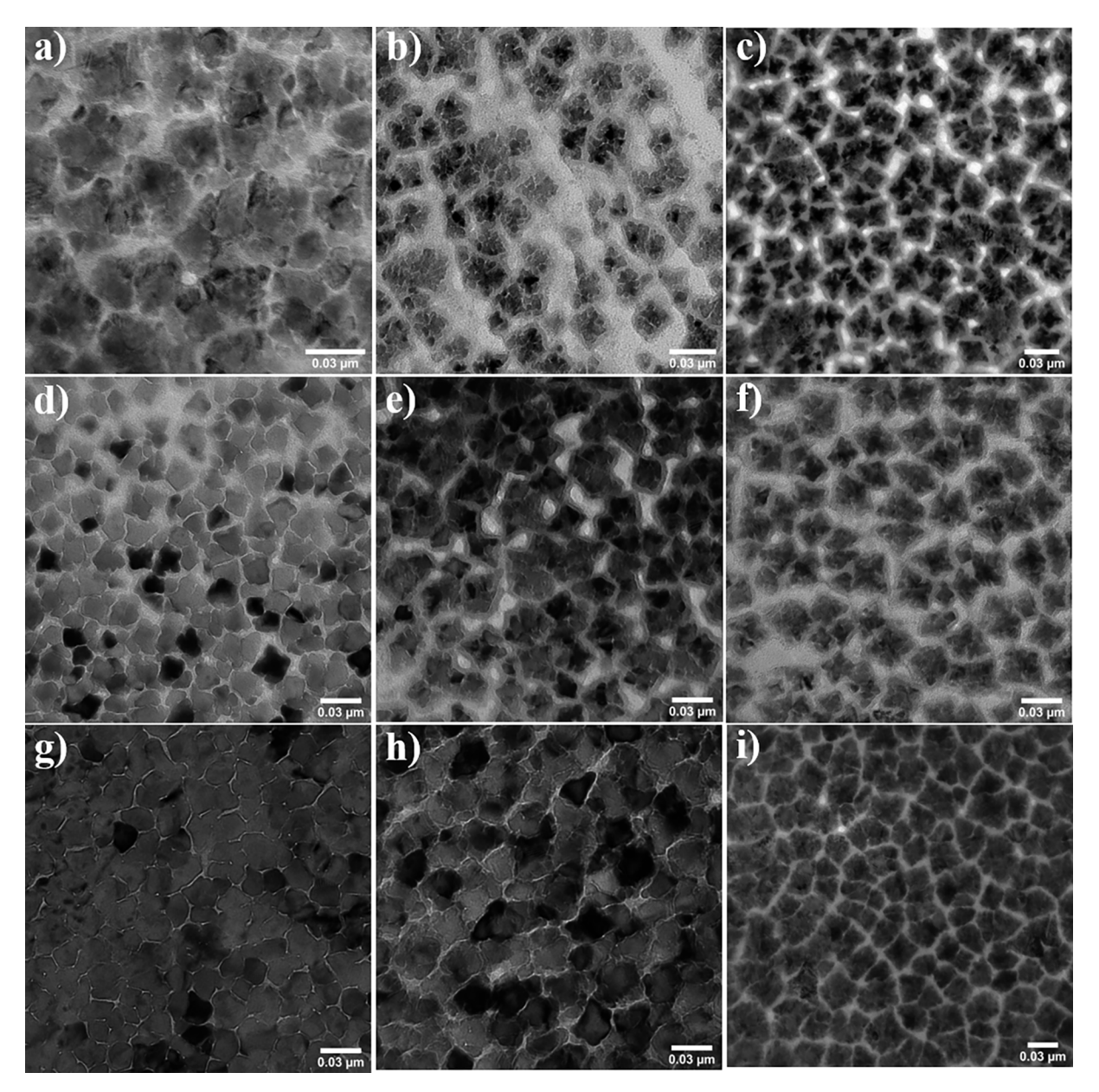


Fig. A.1. Bright field TEM micrographs depicting the voided nature of the films grown at 0.47, 0.67, and 1.33 Pa. (a–c) are films grown at 0.2 nm/s with pressures of 0.47, 0.67, and 1.33 Pa respectively. (g–i) are films grown at 0.1 nm/s with pressures of 0.47, 0.67, and 1.33 Pa respectively. (g–i) are films grown at 0.1 nm/s with pressures of 0.47, 0.67, and 1.33 Pa respectively.

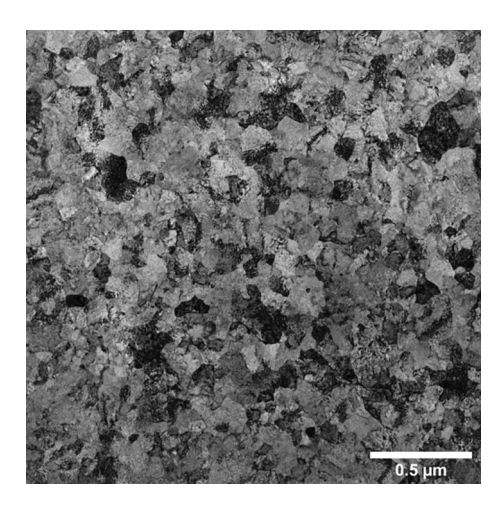


Fig. A.2. Representative bright field TEM micrograph of the films grown at 0.27 Pa. Note the fully consolidated nature of the film.

References

- [1] D. Choi, B. Wang, S. Chung, X. Liu, A. Darbal, A. Wise, N.T. Nuhfer, K. Barmak, A. P. Warren, K.R. Coffey, M.F. Toney, Phase, grain structure, stress, and resistivity of sputter-deposited tungsten films, J. Vac. Sci. Technol. A 29 (2011), 051512, https://doi.org/10.1116/1.3622619.
- [2] J. Johnson A, R. Wilkerson, S. DiPietro, G.B. Thompson, Cermet surrogate nuclear fuels from coated powders, J.Nuclear Mater. 557 (2021), https://doi.org/10.1016/ i.jnucmat.2021.153246.
- [3] R.v. Medvedev, A.A. Zameshin, J.M. Sturm, A.E. Yakshin, F. Bijkerk, W/B short period multilayer structures for soft X-rays, AIP Adv. 10 (2020), https://doi.org/ 10.1063/1.5143397.
- [4] Toivo T. Kodas, M.J. Hampden-Smith, The Chemistry of Metal CVD, VCH, 1994.
- [5] Q. Hao, W. Chen, G. Xiao, Beta (β) tungsten thin films: structure, electron transport, and giant spin Hall effect, Appl. Phys. Lett. 106 (2015), https://doi.org/10.1063/14.010867
- [6] T. Karabacak, A. Mallikarjunan, J.P. Singh, D. Ye, G.C. Wang, T.M. Lu, β-Phase tungsten nanorod formation by oblique-angle sputter deposition, Appl. Phys. Lett. 83 (2003) 3096–3098, https://doi.org/10.1063/1.1618944.
- [7] F.T.N. Vüllers, R. Spolenak, Alpha- vs. beta-W nanocrystalline thin films: a comprehensive study of sputter parameters and resulting materials' properties, Thin Solid Films 577 (2015) 26–34, https://doi.org/10.1016/j.tsf.2015.01.030.
- [8] E.A.I. Ellis, M. Chmielus, S.P. Baker, Effect of sputter pressure on ta thin films: beta phase formation, texture, and stresses, Acta Mater. 150 (2018) 317–326, https:// doi.org/10.1016/j.actamat.2018.02.050.
- [9] E.A.I. Ellis, M. Chmielus, S. Han, S.P. Baker, Effect of sputter pressure on microstructure and properties of β-Ta thin films, Acta Mater. 183 (2020) 504–513, https://doi.org/10.1016/j.actamat.2019.10.056.
- [10] R. Koch, The intrinsic stress of polycrystalline and epitaxial thin metal films, 1994.
- [11] M. Ohring, Materials Science of Thin Films, second ed., Academic Press, San Diego, 2002.
- [12] M.-W. Moon, J.-W. Chung, K.-R. Lee, K.H. Oh, R. Wang, A.G. Evans, An experimental study of the influence of imperfections on the buckling of compressed thin films, Acta Mater. 50 (2002) 1219–1227.
- [13] G. Abadias, E. Chason, J. Keckes, M. Sebastiani, G.B. Thompson, E. Barthel, G. L. Doll, C.E. Murray, C.H. Stoessel, L. Martinu, Review article: stress in thin films and coatings: current status, challenges, and prospects, J. Vac. Sci. Technol. A 36 (2018), 020801, https://doi.org/10.1116/1.5011790.
- [14] R.W. Hoffman, Stresses in thin films: the relevance of grain boundaries and impurities, Thin Solid Films 34 (1976) 185–190.
- [15] F. Spaepen, INTERFACES AND STRESSES IN THIN FILMS p, n.d. www.elsevier. com/locate/actamat.
- [16] C. Friesen, S.C. Seel, C.v. Thompson, Reversible stress changes at all stages of Volmer-Weber film growth, J. Appl. Phys. 95 (2004) 1011–1020, https://doi.org/ 10.1063/1.1637728.
- [17] C.W. Pao, S.M. Foiles, E.B. Webb, D.J. Srolovitz, J.A. Floro, Thin film compressive stresses due to adatom insertion into grain boundaries, Phys. Rev. Lett. 99 (2007), https://doi.org/10.1103/PhysRevLett.99.036102.
- [18] E. Chason, B.W. Sheldon, L.B. Freund, J.A. Floro, S.J. Hearne, Origin of compressive residual stress in polycrystalline thin films, Phys. Rev. Lett. 88 (2002) 4, https://doi.org/10.1103/PhysRevLett.88.156103.
- [19] G. Carter, Peening in ion-assisted thin-film deposition: a generalized model, J. Phys. D. Appl. Phys. 27 (1994) 1046.
- [20] D. Magnfält, A. Fillon, R.D. Boyd, U. Helmersson, K. Sarakinos, G. Abadias, Compressive intrinsic stress originates in the grain boundaries of dense refractory polycrystalline thin films, J. Appl. Phys. 119 (2016), https://doi.org/10.1063/ 1.4941271

- [21] E. Chason, J.W. Shin, S.J. Hearne, L.B. Freund, Kinetic model for dependence of thin film stress on growth rate, temperature, and microstructure, J. Appl. Phys. 111 (2012), https://doi.org/10.1063/1.4704683.
- [22] E. Chason, M. Karlson, J.J. Colin, D. Magnfält, K. Sarakinos, G. Abadias, A kinetic model for stress generation in thin films grown from energetic vapor fluxes, J. Appl. Phys. 119 (2016), https://doi.org/10.1063/1.4946039.
- [23] T. Kaub, Z. Rao, E. Chason, G.B. Thompson, The influence of deposition parameters on the stress evolution of sputter deposited copper, Surf. Coat. Technol. 357 (2019) 939–946, https://doi.org/10.1016/j.surfcoat.2018.10.059.
- [24] T.R. Koenig, Z. Rao, E. Chason, G.J. Tucker, G.B. Thompson, The microstructural and stress evolution in sputter deposited Ni thin films, Surf. Coat. Technol. 412 (2021), https://doi.org/10.1016/j.surfcoat.2021.126973.
- [25] A. Fillon, G. Abadias, A. Michel, C. Jaouen, Stress and microstructure evolution during growth of magnetron-sputtered low-mobility metal films: influence of the nucleation conditions, Thin Solid Films (2010) 1655–1661, https://doi.org/ 10.1016/j.tsf.2010.07.091.
- [26] P. Petroff, T.T. Sheng, A.K. Sinha, G.A. Rozgonyi, F.B. Alexander, Microstructure, growth, resistivity, and stresses in thin tungsten films deposited by rf sputtering, J. Appl. Phys. 44 (1973) 2545–2554, https://doi.org/10.1063/1.1662611.
- [27] R.C. Sun, T.C. Tisone, P.D. Cruzan, The origin of internal stress in low-voltage sputtered tungsten films, J. Appl. Phys. 46 (1975) 112–117, https://doi.org/ 10.1063/1.322250.
- [28] T.J. Vink, W. Walrave, J.L.C. Daams, A.G. Dirks, M.A.J. Somers, K.J.A. van den Aker, Stress, strain, and microstructure in thin tungsten films deposited by dc magnetron sputtering, J. Appl. Phys. 74 (1993) 988–995, https://doi.org/10.1063/ 1.354842.
- [29] Y.G. Shen, Y.W. Mai, Q.C. Zhang, D.R. McKenzie, W.D. McFall, W.E. McBride, Residual stress, microstructure, and structure of tungsten thin films deposited by magnetron sputtering, J. Appl. Phys. 87 (2000) 177–187, https://doi.org/10.1063/ 1.371841.
- [30] T. Kaub, G.B. Thompson, Ti segregation in regulating the stress and microstructure evolution in W-Ti nanocrystalline films, J. Appl. Phys. 122 (2017), https://doi.org/ 10.1063/1.4991880.
- [31] G.G. Stoney, The tension of metallic films deposited by electrolysis, Proc. R. Soc. A (1909) 172–175, https://doi.org/10.1098/rspa.1909.0021.
- [32] A.M. Engwall, S.J. Shin, J. Bae, Y.M. Wang, Enhanced properties of tungsten films by high-power impulse magnetron sputtering, Surf. Coat. Technol. 363 (2019) 191–197, https://doi.org/10.1016/j.surfcoat.2019.02.055.
- [33] L.A. Giannuzzi, F.A. Stevie, A review of focused ion beam milling techniques for TEM specimen preparation, n.d, www.elsevier.com/locate/micron.
- [34] K. Barmak, J. Liu, Impact of deposition rate, underlayers, and substrates on β-tungsten formation in sputter deposited films, J. Vac. Sci. Technol. A 35 (2017), 061516, https://doi.org/10.1116/1.5003628.
- [35] J.A. Thornton, High rate thick film growth, Ann. Rev. Mater. Sci. 7 (1977) 239–260.
- [36] A. Chargui, R. el Beainou, A. Mosset, S. Euphrasie, V. Potin, P. Vairac, N. Martin, Influence of thickness and sputtering pressure on electrical resistivity and elastic wave propagation in oriented columnar tungsten thin films, Nanomaterials 10 (2020), https://doi.org/10.3390/nano10010081.
- [37] S. Taheriniya, S.S. Parhizgar, A.H. Sari, Investigating the effect of sputtering conditions on the physical properties of aluminum thin film and the resulting alumina template, Results Phys. 9 (2018) 1428–1435, https://doi.org/10.1016/j. rinp.2018.03.060.
- [38] P. Catania, R.A. Roy, J.J. Cuomo, Phase formation and microstructure changes in tantalum thin films induced by bias sputtering, J. Appl. Phys. 74 (1993) 1008–1014, https://doi.org/10.1063/1.354946.

- [39] I.A. Weerasekera, S.I. Shah, D.v. Baxter, K.M. Unruh, Structure and stability of sputter deposited beta-tungsten thin films, Appl. Phys. Lett. 64 (1994) 3231–3233, https://doi.org/10.1063/1.111318.
- [40] A. Chattaraj, M. Balal, A.K. Yadav, S.R. Barman, A.K. Sinha, S.N. Jha, S. Joulie, V. Serin, A. Claverie, V. Kumar, A. Kanjilal, Unravelling oxygen driven α to β phase
- transformation in tungsten, Sci. Rep. 10 (2020), https://doi.org/10.1038/s41598-020-71650-2
- [41] J.J. Colin, G. Abadias, A. Michel, C. Jaouen, On the origin of the metastable β -Ta phase stabilization in tantalum sputtered thin films, Acta Mater. 126 (2017) 481–493, https://doi.org/10.1016/j.actamat.2016.12.030.